# Birefringence Control Using Stress Engineering in Silicon-on-Insulator (SOI) Waveguides

Winnie N. Ye, Dan-Xia Xu, Siegfried Janz, Pavel Cheben, Marie-Josée Picard, Boris Lamontagne, and N. Garry Tarr

***Abstract*—We demonstrate that stress engineering is an effective tool to modify or eliminate polarization dispersion in silicon-on-insulator (SOI) waveguide devices, for a wide range of waveguide cross-section shapes and dimensions. The stress-induced effects on the modal birefringence of SOI waveguides are investigated numerically and experimentally. Finite-element simulations show that while the birefringence of ridge waveguides with both slanted and vertical sidewalls can be effectively modified using cladding stress, the birefringence becomes much less sensitive to dimension fluctuations with decreasing sidewall slope. To efficiently simulate the stress-induced effects we propose a normalized plane-strain model which can achieve comparable accuracy as a fully generalized plane-strain model but requires significantly less computational resources. Excellent agreement is achieved between the calculated and measured birefringence tuning using $SiO_2$ cladding induced stress. Finally, both calculations and experiments confirm that cladding induced stress can be used to eliminate the birefringence in SOI waveguides of arbitrary shapes, for typical $SiO_2$ film stress values ($\sigma_{\rm film} \approx -100$ to $-300$ MPa) and cladding thicknesses of the order of 1 $\mu$m or less.**

***Index Terms*—Arrayed waveguide grating (AWG), birefringence, silicon-on-insulator (SOI), strain, stress, waveguides.**

## I. Introduction

SILICON-ON-INSULATOR (SOI) is a promising platform for making multifunctional and high-density integrated optic devices. The mature silicon microfabrication technologies have established a firm foundation for making low-cost and compact integrated photonics devices. Furthermore, the high refractive index contrast between the cladding and the waveguide core facilitates the confinement and guiding of light in structures with micron or submicron dimensions. However, the high index contrast makes the control of waveguide birefringence extremely challenging. The research in birefringence control is driven primarily by the requirement of polarization insensitivity in interferometric devices such as arrayed waveguide gratings (AWGs) and switches for telecommunication applications.

In an SOI waveguide, light is guided in a silicon core separated from the silicon substrate by an $SiO_2$ layer acting as the lower cladding. Fig. 1 shows the geometry of a typical SOI trapezoidal ridge (with slanted-sidewalls) waveguide with an $SiO_2$ upper cladding layer. Simulations have shown that the thickness of the lower $SiO_2$ cladding does not have a significant effect on the effective index of the waveguide. The "cladding" in this paper refers to the upper cladding, unless specified otherwise.

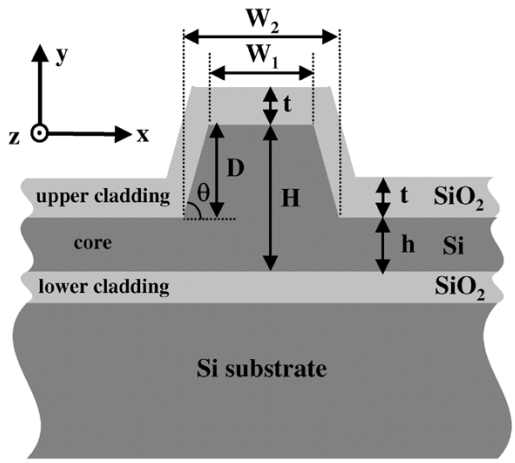


Fig. 1. The cross section of a ridge waveguide in an SOI platform. The upper $SiO_2$ cladding has a thickness $t$, the ridge height is $H$, the etch depth $D$ is $(H-h)$, $W_1$, and $W_2$ are the top and bottom ridge widths, respectively, and $\theta$ is the ridge sidewall angle.

Waveguide birefringence is defined as the difference between the effective indexes of the two orthogonally polarized waveguide modes: the out-of-plane polarized TM mode (electric field along $y$ axis in Fig. 1) and the in-plane polarized TE mode (electric field along $x$); that is, $\Delta n_{\rm eff} = n_{\rm eff}^{\rm TM} - n_{\rm eff}^{\rm TE}$. Waveguide birefringence consists of geometrical birefringence $(\Delta n_{\rm geo})$ and stress-induced birefringence $(\Delta n_{\rm stress})$ : $\Delta n_{\rm eff} = \Delta n_{\rm geo} + \Delta n_{\rm stress}$. The former is the consequence of an axially asymmetric waveguide cross section [1], while the latter is produced by an anisotropic stress in the core due to the photoelastic effect. The waveguide core geometry influences not only the modal birefringence, but also other critical performance parameters such as the number of modes, mode sizes, and minimum bend radius. Although in principle, the birefringence-free and single-mode conditions can be simultaneously achieved for waveguides with large cross sections by adjusting the core geometry [2], previous studies ([3], [4]) have shown that such technique is not practical for waveguides with dimensions in the order of a micron. The low tolerance to dimensional fluctuations arising from fabrication processes poses a challenging technical problem. This paper describes the use of cladding stress to control the waveguide birefringence. We demonstrate that by incorporating stress into the waveguide design, the waveguide birefringence can be decoupled from the geometrical constraints.

Manuscript received June 25, 2004; revised September 15, 2004. This work was supported by the National Science and Engineering Research Council (NSERC) and the National Research Council of Canada (NRC).

W. N. Ye and N. G. Tarr are with the Department of Electronics, Carleton University, Ottawa, ON K1S 5B6, Canada (e-mail: winnie.ye@nrc-cnrc.gc.ca).

D.-X. Xu, S. Janz, P. Cheben, M.-J. Picard, and B. Lamontagne are with the Institute for Microstructural Sciences, National Research Council of Canada, Ottawa, ON K1A 0R6, Canada.

Digital Object Identifier 10.1109/JLT.2005.843518

TABLE I
MATERIAL PARAMETERS OF Si (SUBSTRATE AND WAVEGUIDE CORE) AND $SiO_2$ (UPPER AND LOWER CLADDINGS)

| Material | Young's modulus, $E$ (GPa) | Poisson's ratio, $\nu$ | Thermal expansion coefficient, $\alpha$ ($K^{-1}$) | Refractive index[a] $n$ | Photoelastic tensor elements[b] [5] $p_{11}$ | $p_{12}$ |
|---|---|---|---|---|---|---|
| Si | 130 | 0.27 | $3.6 \times 10^{-6}$ | 3.476 | -0.101 | 0.0094 |
| $SiO_2$ | 76.7 | 0.186 | $5.40 \times 10^{-7}$ | 1.444 | 0.16 | 0.27 |

[a]Measured at wavelength $\lambda = 1550$ nm
[b]Measured at wavelength $\lambda = 1150$ nm

This paper is organized as follows. In Section II, the photoelastic relations in waveguides are reviewed, and the generalized plane-strain and ordinary plane-strain approximations for stress calculations are compared. We also present the derivations of a normalized plane-strain calculation scheme: a new model that is much simpler than the generalized model, yet yields more accurate results than the ordinary plane-strain model. In Section III, the stress-induced effects on modal birefringence are investigated for two types of waveguide profiles: the rectangular (vertical-sidewalled), and the trapezoidal (slanted-sidewalled) SOI ridge waveguides. The numerical results of birefringence tuning for these two profile types are compared. Section IV presents the experimental results which confirm that stress engineering is an effective and practical tool to control waveguide birefringence.

## II. WAVEGUIDE STRESS AND STRAIN: THEORY

Stress in a waveguide is determined by both the mismatch in the thermal expansion coefficients of the different layers (among upper and lower claddings, core, and substrate) and the waveguide geometry. In an SOI ridge waveguide as shown in Fig. 1, the stress in the $SiO_2$ upper cladding film produces a stress distribution within and near the embedded Si ridge, which in turn causes a change in the refractive index in both the Si and $SiO_2$ layers via the photoelastic effect. The stress-induced change in material refractive index can be described by the following relations [1], [6]

$$\begin{aligned} \Delta n_x &= n_x - n_0 = -C_1\sigma_x - C_2(\sigma_y + \sigma_z) \\ \Delta n_y &= n_y - n_0 = -C_1\sigma_y - C_2(\sigma_x + \sigma_z) \end{aligned} \tag{1}$$

where $\sigma_x, \sigma_y$, and $\sigma_z$ are the principal stress tensor components along the $x$, $y$, and $z$ axis directions, respectively; $n_0$ is the refractive index of the material without stress; and $C_1$ and $C_2$ are the stress-optical constants, related to the Young's modulus $(E)$, Poisson's ratio $(\nu)$, and the photoelastic tensor elements ($p_{11}$ and $p_{12}$) [1], [6] as

$$\begin{aligned} C_1 &= \frac{n^3}{2E}(p_{11} - 2\nu p_{12}) \\ C_2 &= \frac{n^3}{2E}[-\nu p_{11} + (1-\nu)p_{12}]. \end{aligned} \tag{2}$$

Both the material refractive index and the photoelastic tensor elements depend on the wavelength; hence, the stress-optical constants $C_1$ and $C_2$ are also wavelength dependent. In this paper, the operating wavelength is assumed to be $\lambda = 1550$ nm. Table I summarizes the material parameters used in our simulations. Since the photoelastic tensor elements $(p_{ij})$ were measured at 1150 nm, the stress-optical constants derived from them may not be accurate at 1550 nm. However, the dispersion in $p_{ij}$ is expected to be weak since the strong electronic transitions occur at much shorter wavelengths for both Si and $SiO_2$.

The modeled SOI waveguide system consists of a silicon substrate, a buried $SiO_2$ layer, an Si waveguide layer including an etched ridge waveguide, and an overlying $SiO_2$ cladding. The structure is assumed to be invariant along the waveguide propagation direction. The model system was set to be 100 $\mu$m wide—large enough that edge effects do not distort the stress distribution in the vicinity of the ridge waveguide. The boundary conditions are chosen such that the top, bottom, and sides of the model system are surfaces that can move freely in response to internal stresses. In our calculations, we assume that all the material layers are at equilibrium at a reference temperature $(T_{\text{ref}})$, which corresponds to the deposition temperature for an idealized oxide film on a silicon system. As a result, there is no intrinsic stress in any layer at the reference temperature.

The strain and stress components are related as follows, given the difference between the operating and reference temperatures $(\Delta T = T_0 - T_{\text{ref}})$

$$\begin{bmatrix} \varepsilon_x \\ \varepsilon_y \\ \varepsilon_z \end{bmatrix} = \frac{1}{E}\left( \begin{bmatrix} 1 & -\nu & -\nu \\ -\nu & 1 & -\nu \\ -\nu & -\nu & 1 \end{bmatrix} \begin{bmatrix} \sigma_x \\ \sigma_y \\ \sigma_z \end{bmatrix} \right) + \alpha \Delta T \tag{3}$$

where $\varepsilon_x, \varepsilon_y$, and $\varepsilon_z$ correspond to the principal strain along the $x, y$, and $z$ directions, respectively. According to (3), the strain consists of two parts: the elastic strain (first term) and the thermal-induced strain (second term). By inverting (3), an expression for the stress distribution tensors $(\sigma_i)$ can be obtained as in (4).

$$\begin{bmatrix} \sigma_x \\ \sigma_y \\ \sigma_z \end{bmatrix} = \frac{E}{(1+\nu)(1-2\nu)} \begin{bmatrix} 1-\nu & \nu & \nu \\ \nu & 1-\nu & \nu \\ \nu & \nu & 1-\nu \end{bmatrix} \begin{bmatrix} \varepsilon_x \\ \varepsilon_y \\ \varepsilon_z \end{bmatrix} - \frac{\alpha E \Delta T}{1-2\nu}. \tag{4}$$

The stress field in the waveguide is numerically solved by the finite-element method (FEM) using a commercial software package (FEMLAB). FEMLAB solves the static equilibrium equation, which simultaneously satisfies the stress–strain relation, the thermal effects, and the stain-displacement relation, with proper boundary conditions, for the displacement variables in the $x$, $y$, and $z$ directions. Once the stress distribution in the vicinity of the ridge waveguide is known, the local refractive index distribution can be evaluated using (1). The FEM is also used to solve Maxwell's equations for both the TE- and TM-like waveguide mode distributions and the corresponding effective index values $n_{\text{eff}}$. The mesh density (the number of elements) used in simulations is over 38 000 for a computation window

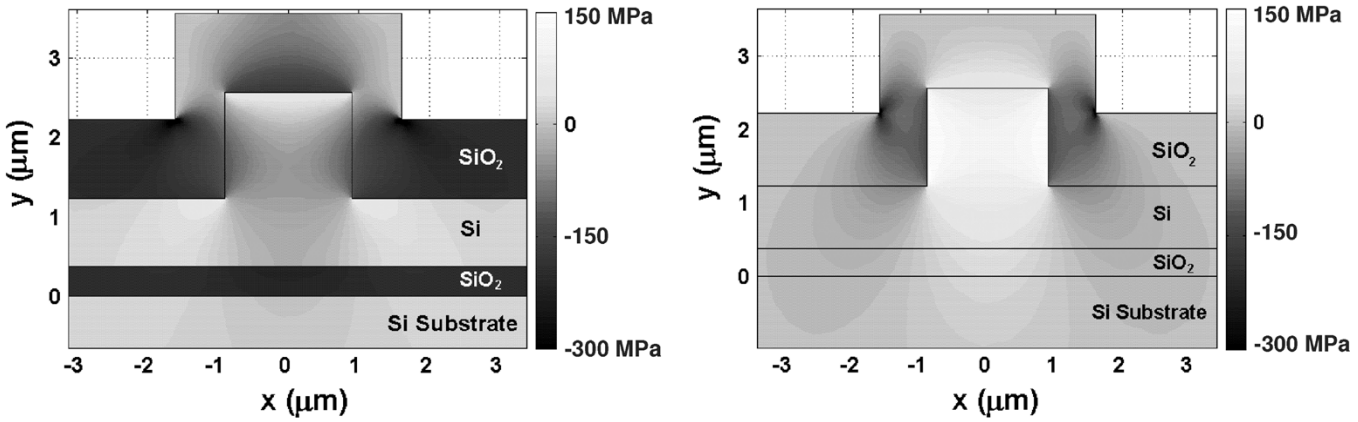


Fig. 2. The $x$ and $y$ components of the stress distributions in an SOI ridge waveguide. (a) Stress field $\sigma_x$. (b) Stress field $\sigma_y$. The buried oxide layer thickness is 0.37 $\mu$m, the upper oxide cladding thickness is 1 $\mu$m, and Si ridge height and width are 2.2 and 1.83 $\mu$m, respectively.

size of 8 $\mu$m $\times$ 3 $\mu$m, with a maximum element area of around 625 nm$^2$.

We define $\sigma_{\rm film}$ as the in-plane stress component (in $x$ direction, $\sigma_x$) that is present in the uniform upper cladding film, far away from the ridge. In this paper, $\sigma_{\rm film}$ is chosen to characterize the stress in the cladding. The value of the stress level $\sigma_{\rm film}$ can be obtained experimentally from the bow radius of a wafer coated with a stressed film. In comparisons of theoretical results with experiments, the experimentally measured $\sigma_{\rm film}$ is used as the target stress level in the simulation analysis by varying $\Delta T$ in the model system. In the next subsections, we discuss three different plane-strain calculation schemes.

### A. Generalized Plane Strain Model

A generalized plane–strain model assumes that the strain along the waveguide propagation $z$ direction is independent of $z$ but can vary with $x$ and $y$. This model holds for waveguides that are invariant along the propagation direction and are much longer than their cross-section dimensions. In this formulation, the wafer is allowed to deform in response to film stress in the $x$, $y$, or $z$ direction. The strain in the $z$ direction, in the simplest approximation, is constrained to vary linearly in the $x$–$y$ plane. That is

$$\varepsilon_z = \varepsilon_0 + ax + by \tag{5}$$

where $\varepsilon_0, a$, and $b$ are constants. $\varepsilon_0$ depends mainly on the material's thermal expansion coefficient $(\alpha)$ and the temperature change $(\Delta T)$. The value of $b$ is usually much larger than that of $a$ since wafer bending requires that the in-plane strain varies in the $y$ direction across the wafer thickness, while bending should be independent of $x$ and $z$ far from the wafer edges.

Stress distributions in an SOI ridge waveguide, calculated from the generalized plane-strain model using FEM are shown in Fig. 2. The $x$ and $y$ components of the anisotropic stress distribution in the core area contribute to the change in the refractive index in the Si core, as described in (1). The positive and negative values of the stress represent the tensile and compressive forces, respectively. The stress in a uniform $SiO_2$ film deposited on Si typically ranges from $\sigma_{\rm film} = -100$ to $-400$ MPa, depending on deposition conditions and film thickness. As shown in Fig. 2, a compressive cladding stress along the $x$ direction induces an anisotropic stress in the core: a compressive stress in the $x$ direction and a tensile stress in the $y$ direction. The influence of stress on waveguide birefringence will be discussed in Section III.

### B. Ordinary Plane Strain Model

One of the main drawbacks associated with using the fully generalized plane-strain model is that for a system large enough to avoid edge effects, but with a fine enough mesh to accurately calculate the stress fields, the calculation takes a long time and requires a large computation memory. This model can be simplified by assuming that the strain component along the propagation $z$ direction is negligible compared to strains in $x$ and $y$ directions [7]. Under this plane-strain assumption, the model system is not allowed to either expand or contract in $z$ direction (i.e., $\varepsilon_z = 0$). The three-dimensional (3-D) stress analysis (4) is reduced to the equations

$$\begin{aligned}
\sigma_x &= \frac{E}{(1+\nu)(1-2\nu)}[(1-\nu)\epsilon_x + \nu\epsilon_y] - \frac{\alpha E \Delta T}{1-2\nu} \\
\sigma_y &= \frac{E}{(1+\nu)(1-2\nu)}[\nu\epsilon_x + (1-\nu)\epsilon_y] - \frac{\alpha E \Delta T}{1-2\nu} \\
\sigma_z &= \nu(\sigma_x + \sigma_y) - \alpha E \Delta T.
\end{aligned} \tag{6}$$

Here the equations for $\sigma_x$ and $\sigma_y$ are decoupled from $\sigma_z$, resulting in a simpler 2-D problem for the stress distribution in the $x$–$y$ plane. Although this model has been used to calculate stress in waveguides ([1], [8]–[10]), it introduces a strong tensile stress $\sigma_z$ into the waveguiding Si core and the substrate, but lower compressive stress in the cladding layers along the $z$ axis. These changes in stress cause a uniform shift in the calculated material refractive indexes $n_x$ and $n_y$, which in turn changes the effective indexes of the waveguide modes. This can be important in modeling interference based polarization control devices employing stress.

The artificial stress levels in the Si and the $SiO_2$ layers along $z$ also changes their relative thermal expansion in the $x$–$y$ plane. For example, in the case of a uniform $SiO_2$ film on a thick Si substrate, the expression obtained from (4) (i.e., the generalized plane-strain model) for the in-plane stress $\sigma_{\rm film}$ in the $SiO_2$

TABLE II
COMPARISON OF OXIDE FILM STRESS $\sigma_{\text{film}}$ AND WAVEGUIDE BIREFRINGENCE CALCULATIONS FROM GENERALIZED, ORDINARY, AND NORMALIZED PLANE STRAIN MODELS. THE STRESS VALUES ARE TAKEN AT THE MIDDLE OF THE OXIDE FILM, 4 $\mu$m AWAY FROM THE CENTER OF THE RIDGE WAVEGUIDE. THE SOI WAVEGUIDE HAS THE FOLLOWING DIMENSIONS: $H = 2.2$ $\mu$m, $W = 1.8$ $\mu$m, AND $t = 1$ $\mu$m. THE STRESS CALCULATION WINDOW IS 100 $\mu$m WIDE × 100 $\mu$m THICK. MATERIAL PARAMETERS LISTED IN TABLE I WERE USED FOR THESE CALCULATIONS

| Etch Depth | Model | $\sigma_x$ (MPa) | $\sigma_y$ (MPa) | $\sigma_z$ (MPa) | Birefringence $\Delta n_{\text{eff}}$ | % change in $\Delta n$ |
|---|---|---|---|---|---|---|
| $D = 1.2$ $\mu$m | Generalized Plane Strain (GPS) Model | -269 | 0.02 | -273 | 0.002334 | - |
| | Ordinary Plane Strain (OPS) Model | -291 | 0.02 | -13.5 | 0.002597 | (+11.27%) |
| | Normalized Plane Strain (NPS) Model | -269 | 0.02 | -280 | 0.002327 | (-0.31%) |
| $D = 1.34$ $\mu$m | GPS Model | -269 | 0.02 | -273 | 0.003651 | - |
| | OPS Model | -291 | 0.02 | -13.5 | 0.003960 | (+8.47%) |
| | NPS Model | -268 | 0.02 | -280 | 0.003643 | (-0.22%) |
| $D = 1.5$ $\mu$m | GPS Model | -269 | 0.02 | -273 | 0.004903 | - |
| | OPS Model | -291 | 0.02 | -13.4 | 0.005254 | (+7.16%) |
| | NPS Model | -268 | 0.02 | -280 | 0.004894 | (-0.18%) |

cladding, allowing unconstrained thermal expansion in all directions is

$$\sigma_{\text{film}} = \sigma_x = (\alpha_s - \alpha)\frac{E}{1-\nu}\Delta T \tag{7}$$

where $\alpha_s$ and $\alpha$ are the thermal expansion coefficients of the Si substrate and $SiO_2$, respectively. On the other hand, in the ordinary plane-strain model described by (6), the effective in-plane stress in $x$ axis is given by

$$\sigma_{\text{film}} = \left(\frac{1+\nu_s}{1+\nu}\alpha_s - \alpha\right)\frac{E}{1-\nu}\Delta T. \tag{8}$$

Evaluating these two expressions, the ordinary plane-strain model overestimates the film stress $\sigma_{\text{film}}$ by approximately 10%, and therefore the stress induced birefringence by a similar amount.

### C. Normalized Plane Strain Model

In this section, we present a modified form of the ordinary plane-strain model that correctly reproduces the stress component along the propagation $z$ axis. This simple normalized plane-strain model achieves comparable accuracy as the fully generalized plane-strain model presented in Section II-A. If we neglect wafer bending along the $z$ axis (the bending effects will be discussed later) and assume that the top layers conform to the substrate during cooling, the strain component in the $z$ direction takes the form of $\varepsilon_z = \alpha_s \Delta T$, without the $x$ and $y$ dependency in (5). This approximation assumes the waveguide displacement in the $z$-direction is determined by the thermal expansion of the substrate. This plane-strain model yields the stress–strain relation as follows:

$$\begin{aligned}
\sigma_x' &= \frac{E}{(1+\nu)(1-2\nu)}[(1-\nu)\epsilon_x + \nu\epsilon_y] \\
&\quad - \left(\alpha - \frac{\nu}{1+\nu}\alpha_s\right)\frac{E\Delta T}{1-2\nu} \\
\sigma_y' &= \frac{E}{(1+\nu)(1-2\nu)}[\nu\epsilon_x + (1-\nu)\epsilon_y] \\
&\quad - \left(\alpha - \frac{\nu}{1+\nu}\alpha_s\right)\frac{E\Delta T}{1-2\nu} \\
\sigma_z' &= \nu(\sigma_x' + \sigma_y') - (\alpha - \alpha_s)E\Delta T.
\end{aligned} \tag{9}$$

Comparing (9) to (6), the equations for $\sigma_x'$ and $\sigma_y'$ are again decoupled from $\sigma_z'$. Furthermore, the normalized plane-strain (9) for $\sigma_x'$ and $\sigma_y'$ are identical to the ordinary plain strain equations for the stress fields $\sigma_x$ and $\sigma_y$ as in (6), if a normalized thermal expansion coefficient in each layer $\alpha'$ is adopted

$$\alpha' = \alpha - \frac{\nu}{1+\nu}\alpha_s. \tag{10}$$

Solving an ordinary plane-strain problem using (6) with $\alpha'$ will shift the value for $\sigma_z$ in each layer by a constant amount. However, since the resulting difference in $\sigma_z$ is just a uniform constant in each layer, the correct value for $\sigma_z'$ is obtained by adding a constant correction term to $\sigma_z$

$$\sigma_z' = \sigma_z + \frac{E}{1+\nu}\alpha_s \Delta T \tag{11}$$

where the stress field $\sigma_z$ is calculated as in (6), with the inclusion of (10) as the thermal expansion coefficients. This means that the ordinary plane-strain algorithm can be used as before to evaluate the $x$ and $y$ components of the stress distribution in the waveguides, using the normalized thermal expansion coefficients.

Table II compares the numerical results of the waveguide birefringence and the stress $\sigma_{\text{film}}$ in a 1-$\mu$m-thick upper cladding film obtained from the different plane-strain models. The simulated ridge waveguide has a core height of 2.2 $\mu$m and width of 1.8 $\mu$m. The upper and lower oxide cladding has a thickness of 1 and 0.37 $\mu$m, respectively. The results are compared for different ridge etch depths $D$, assuming $\Delta T = -980°$. Using the generalized plane-strain model as the benchmark, it is shown that the ordinary plane-strain model overestimates the birefringence by about 10% for all the three cases, as expected from (7) and (8). When modeling birefringence in interferometric devices such as AWGs, this birefringence error would produce a wavelength shift ranging from $\Delta\lambda = 0.07$ to 0.15 nm, which represents up to 20% of the WDM channel spacing in an 100 GHz (or 0.8 nm) spaced AWG device. The normalized model, on the other hand, produces virtually identical stress levels and birefringence as the fully generalized model, yet requires an order of magnitude less computation time. This is to our knowledge, the first time this extension of the ordinary plane-strain model has been presented for stress calculations in optical waveguides.

TABLE III
COMPARISON OF OXIDE FILM STRESS $\sigma_{\text{film}}$ AND WAVEGUIDE BIREFRINGENCE CALCULATIONS FROM GENERALIZED AND NORMALIZED PLANE STRAIN MODELS. THE STRESS VALUES ARE TAKEN AT THE MIDDLE OF THE OXIDE FILM, 4 $\mu$m AWAY FROM THE CENTER OF THE RIDGE WAVEGUIDE. YOUNG'S MODULUS OF THE SUBSTRATE WAS SET TO $E_s' = 10^3 E_s$. THE SOI RIDGE WAVEGUIDE HAS THE SAME DIMENSIONS AS IN TABLE II. THE STRESS CALCULATION WINDOW IS REDUCED TO 40 $\mu$m WIDE BY 5 $\mu$m THICK (FROM 100 $\mu$m × 100 $\mu$m AS IN TABLE II)

| Etch Depth | Model | $\sigma_x$ (MPa) | $\sigma_y$ (MPa) | $\sigma_z$ (MPa) | Birefringence $\Delta n_{\text{eff}} = n_{\text{eff}}^{\text{TM}} - n_{\text{eff}}^{\text{TE}}$ |
|---|---|---|---|---|---|
| $D = 1.2$ $\mu$m | Generalized Plane Strain (GPS) Model | -281 | 0.05 | -282 | 0.002859 |
| | Normalized Plane Strain (NPS) Model | -281 | 0.05 | -282 | 0.002858 |
| $D = 1.34$ $\mu$m | GPS Model | -282 | 0.02 | -283 | 0.004162 |
| | NPS Model | -282 | 0.02 | -283 | 0.004161 |
| $D = 1.5$ $\mu$m | GPS Model | -282 | 0.04 | -282 | 0.005407 |
| | NPS Model | -282 | 0.04 | -282 | 0.005407 |

### *D. Stress Relief and Calculation Window Size*

Stress relief is an important factor in determining the accuracy of numerical stress calculations for finite systems, and also in comparing theoretical results with experimental measurements. When internal stresses are present, both real and model systems will deform to reduce stress. In the SOI waveguide system, stress relief will occur through bending of the wafer, and through elastic deformations extending inwards from the edges of the wafer and the ridge itself. The magnitude and range of these effects must be understood to correctly choose the calculation window size of the model system, and to assess measurements of film stress and waveguide birefringence on finite substrates.

For a slab SOI system, assuming a substrate with thickness $d$ much larger than the film thickness $t$ (i.e., $d \gg t$), the stress relief in the $SiO_2$ cladding is given by [11]

$$\frac{\Delta\sigma}{\sigma_0} = -\frac{4tE(1-\nu_s)}{dE_s(1-\nu)} \tag{12}$$

where $\Delta\sigma$ is the change in stress associated with bending, and $\sigma_0$ is the stress in the cladding film with no substrate bending. Although this equation is derived for a single layer on a substrate, it is approximately correct for our SOI system provided the film thickness includes both the buried oxide and oxide cladding thickness.

Since the strain $\varepsilon_x$ is virtually identical in the Si waveguide layer and the cladding for large bend radii, the stress relief $\Delta\sigma_w$ in the Si waveguide layer is related to the stress relief in the cladding by a ratio of the elastic constants

$$\Delta\sigma_w = \frac{E_s(1-\nu)}{E(1-\nu_s)}\Delta\sigma = -\frac{4t\sigma_0}{d}. \tag{13}$$

Equations (12) and (13) shows that the film stress in the cladding and waveguide layer may vary significantly if the substrate thickness $d$ is comparable to the film thickness $t$. Stress relief also arises from nonuniform strain relaxation at the edges of our finite model system. In a real system, the Si substrate is thick enough (e.g., 500 $\mu$m) and the edges are so far away from the waveguide that stress relief due to edge effects and wafer bending can be neglected.

In numerical simulations, however, the model system should be as small as possible so that the FEM calculations can be completed in a reasonable amount of time and within the available memory allocation. In the conventional calculation of stress fields using FEM, the model wafer height and width must be large enough that stress relief due to strain relaxation at the sides of the wafer is negligible at the ridge waveguide, and the substrate is thick enough that stress relief from bending does not significantly modify the calculated film and waveguide stresses. Simulations show that the edge induced distortion of the stress field extends almost 50 $\mu$m from the edge of the wafer for a 1-$\mu$m-thick oxide film, requiring that the calculation window be at least 100 $\mu$m wide. Similarly, to minimize stress relief, the wafer thickness must be at least 90 $\mu$m or larger. The typical 100 $\mu$m × 100 $\mu$m window required for an accurate stress calculation is about 400 times larger than the window required for the calculation of the waveguide modes.

The normalized plane-strain model can effectively account for thermal expansion along the $z$ axis ($\varepsilon_z = \alpha_s \Delta T$), but both the ordinary and normalized plane-strain models do not allow bending of the wafer along the $z$ axis because the strain component $\varepsilon_z$ has no dependence on either $x$ or $y$. Therefore stress relief due to wafer bending will not be correctly evaluated (see deviations in calculated stress levels and birefringence from the generalized model in Table II). We can reduce wafer bending and the range of lateral edge effects by artificially setting the Young's modulus of the substrate wafer to a large value $E_s'$. In the limit of a large Young's modulus, the edge distortion of the stress fields extends only about 15 $\mu$m from the edge, while the bending contribution to stress relief is effectively eliminated and the wafer behaves as if it is absolutely rigid. Our calculations confirm that the stress relief effects are negligible for typical substrate thicknesses. Using a Young's modulus of 130 TPa for the substrate ($10^3$ times higher than the typical $E_s$, no wafer bending), the film stress value differs by less than 1% of the expected value for a 500-$\mu$m substrate with typical $E_s$, and less than 5% for a 100-$\mu$m substrate, for oxide thickness of 1 $\mu$m. Since the film stress values are independent of the substrate thickness when a large $E_s'$ is adopted, the model substrate thickness may be reduced from the initial 100 $\mu$m to 5 $\mu$m with no effect on the calculated stress fields in the ridge waveguide.

By using a large $E_s'$ with a thin substrate to reduce system size, the effect of stress relief cannot be reproduced. However, for a given substrate thickness, (12) and (13) can be used to determine a value for $E_s'$ that will produce the same stress relief as for a wafer of a given thickness. Therefore, by using (12) to estimate the bend induced strain that would occur for the real wafer, the effect of stress relief can be modeled by choosing the right combination of model substrate thickness and Young's modulus.

Table III makes a similar comparison as in Table II, except the Young's modulus of the substrate $E_s$ is increased by three orders

of magnitude to 130 TPa. The 100 $\mu$m (wide) by 100 $\mu$m (thick) window for stress calculations used for Table II is reduced to a smaller computation window of 40 $\mu$m $\times$ 5 $\mu$m. The FEM calculations confirm that in the absence of wafer bending (i.e., high Young's modulus $E_s$), the results of the fully generalized plane-strain model and the normalized plane-strain model are in excellent agreement. The increase in birefringence of about 14% in Table III compared with the results in Table II is due to the absence of stress relief $(\Delta\sigma_w)$ in the Si waveguide layer, in the calculations using a stiff substrate.

We conclude that, by using the normalized thermal expansion coefficient $(\alpha')$ in (10) for each layer, combined with the correction term to $\sigma_z$ from (11), the accuracy of the plane-strain model is equivalent to that of the generalized model. By combining the normalized plane-strain model with a high $E_s'$ for the substrate to eliminate stress relief effects, we have been able to reduce the computation time and memory usage required for FEM calculations of the stress induced birefringence by more than two orders of magnitude, while retaining the accuracy of the fully generalized plane-strain model. This model is used for the analysis presented in the next sections.

## III. Geometrical and Stress-Induced Effects on Waveguide Effective Index and Birefringence

Although the stress-induced effects have been studied extensively in glass waveguides, they were only recently investigated systematically in SOI ridge waveguides of rectangular cross sections [12], [13]. In this paper, we compare the SOI rectangular ridge waveguides (with vertical sidewalls) with the trapezoidal ridge waveguides (with slanted sidewalls), typically obtained by using dry and wet etching, respectively. Dry-etch processing, due to its high cost, is usually used when the feature resolution in thin film structures is of a major concern or when deep vertical sidewall etchings are required. Wet-etching, on the other hand, is simple, yet yields resolution sufficient for many waveguide devices. Another important advantage is that the wet-etching tends to produce smoother sidewalls as compared to RIE (reactive ion etching) and thus scattering loss is significantly reduced [13], [14].

We use the FEM to calculate the stress distribution and the effective indexes of the TE- and TM-like polarized modes with and without stress. The thickness of the upper oxide film covering the ridge sidewalls is assumed to be 70% of that on the top of the waveguiding layer, as measured in our upper oxide cladding film deposited by plasma enhanced chemical vapor deposition (PECVD) [13], [15].

### A. Waveguide Cross Section

SOI waveguide cross section can be chosen such that only a single mode is supported by the waveguides. The single-mode condition for SOI ridge waveguides is given by the well-known relationship [16]

$$\frac{W}{H} \leq 0.3 + \frac{r}{\sqrt{1-r^2}}, \quad r \geq 0.5 \tag{14}$$

where $r = h/H$ is the ratio of the slab height $(h)$ adjacent to the ridge, to the Si ridge height $(H)$, and $W$ is the ridge width (see Fig. 1). This condition constrains the available ridge width and etch depth ratios in keeping the waveguide single-mode. The technique of tailoring waveguide cross-section aspect ratio has also been used to eliminate the birefringence for waveguides with relatively large cross sections [2]. However, as shown in Fig. 3, the geometrical birefringence, arising from different boundary conditions for orthogonally polarized modes in an asymmetric waveguide, increases exponentially and becomes very sensitive to the errors in the waveguide dimensions, as the waveguide core size scales down below about 2 $\mu$m. This finding can be generalized also for waveguides of arbitrary cross sections. Fig. 3 illustrates that controlling birefringence by tailoring waveguide cross-section aspect ratio becomes difficult in waveguides with small cores. It is noted that our analyses are not limited to single moded waveguides [$W/H$ ratio may not satisfy the relationship in (14)]. The waveguide bending radius can be designed to filter out the unwanted higher waveguide modes [3].

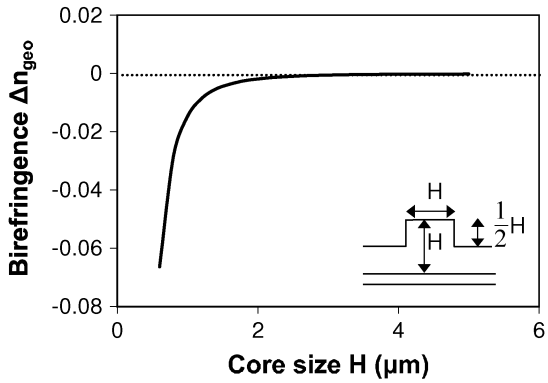


Fig. 3. The influence of core dimensions on waveguide geometrical birefringence $(\Delta n_{\rm geo})$ for a geometry shown in the inset.

For waveguide structures with similar etch depth and core thickness but different cross sections (e.g., rectangular or trapezoidal), the optical properties can still be significantly different. For example, the birefringence of a rectangular ridge waveguide is more susceptible to changes in the ridge geometry (width and etch depth) as compared to a trapezoidal waveguide with similar cross-section area. Fig. 4 shows the electric field contours of the fundamental TE mode in a rectangular [Fig. 4(a)] and a trapezoidal [Fig. 4(b)] ridge waveguide. The abrupt changes in the mode shape due to the sharp inner corners of the rectangular waveguide core contrast distinctively with much smoother field contours in the trapezoidal waveguide.

In Fig. 5, the geometrical birefringence is plotted as a function of ridge sidewall slope for varying etch depths of 1.3, 1.5, and 2 $\mu$m. The sidewall slopes of a fabricated waveguide are determined by the specific etching technique and waveguide orientation with respect to the crystallographic planes. In practice, it is not trivial to tune the sidewall angles. Here we limit our discussion to a theoretical influence of sidewall slope angles on waveguide birefringence. For a given etch depth, the rate of change in waveguide birefringence $(\partial(\Delta n)/\partial\theta)$ increases with the ridge sidewall slope $\theta$. Waveguides with smaller sidewall slopes have better birefringence stability to etch depth errors; however, these waveguides have relatively large birefringence. As shown in Fig. 5, the etch depth plays a critical role in determining birefringence, especially for ridges with large sidewall slopes.

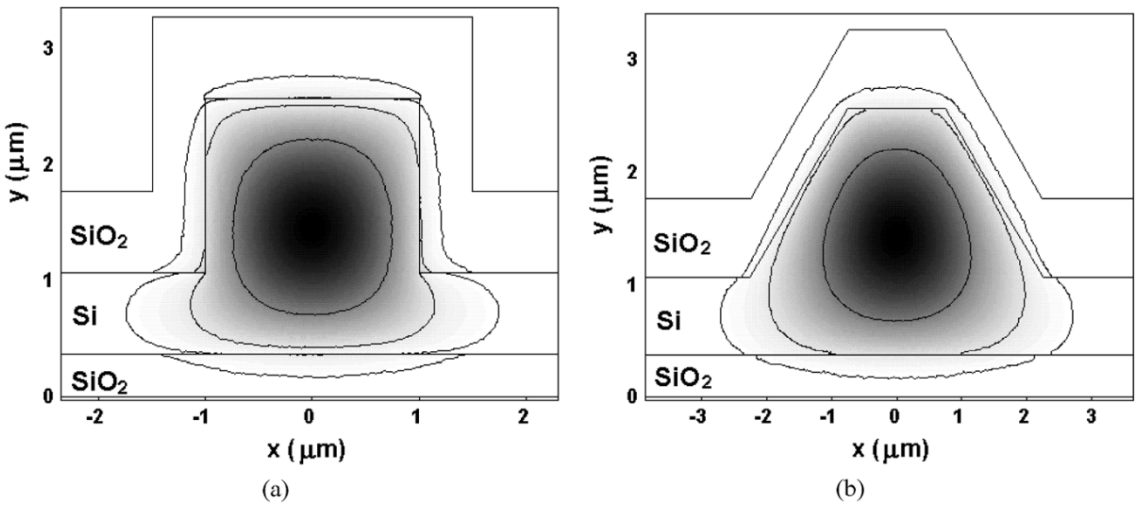


Fig. 4. Fundamental TE mode shapes with equal electric field contours (0.5, 0.1, and 0.01 of the maximum fields) in SOI ridge waveguide The ridge height is 2.2 $\mu$m, the etch depth is 1.5 $\mu$m. (a) Rectangular ridge with a width of 2 $\mu$m. (b) Trapezoidal ridge with a top width $W_1$ of 1.5 $\mu$m and a sidewall angle of 54°.

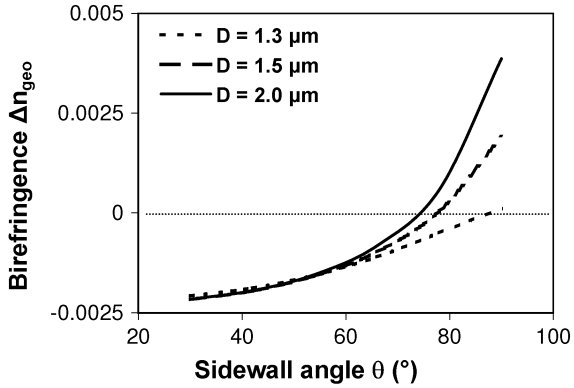


Fig. 5. Ridge sidewall slope $(\theta)$ influence on waveguide geometrical birefringence $(\Delta n_{\rm geo})$ for 3 different etch depths $(D)$. The Si ridge has an upper width $(W_1)$ of 1.5 $\mu$m and the total height of the core is 2.2 $\mu$m.

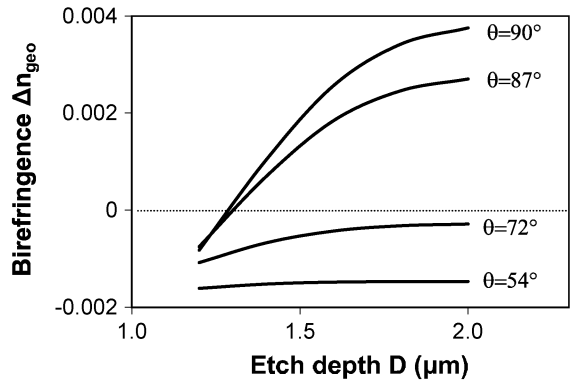


Fig. 6. Etch depth influence on waveguide geometrical birefringence $(\Delta n_{\rm geo})$ for rectangular and trapezoidal waveguides with sidewall slope of 54°, 72°, 87°, and 90°, geometrical effects only (no stress). The Si ridge has a height $H$ of 2.2 $\mu$m and a top ridge width $W_1$ of 1.5 $\mu$m (bottom ridge width $W_2$ varies according to slope $\theta$).

The influence of etch depth on birefringence is further shown in Fig. 6 for four different sidewall angles: 54°, 72°, 87°, and 90°, with a fixed upper ridge width $W_1$ of 1.5 $\mu$m and ridge height $H$ of 2.2 $\mu$m. Dry-etching generally produces nearly vertical sidewalls $(90° \pm 3°)$, while the wet-etching yields approximately 54° sidewalls (angle between Si crystal $\langle 111 \rangle$ and $\langle 100 \rangle$ planes). In the calculations, we use the experimentally measured 87° and 90° sidewall angles for rectangular ridge waveguides, and 54° (and 72°) for trapezoidal waveguides.

Again, it is observed that the birefringence is less sensitive to changes in etch depth for waveguides with trapezoidal cross sections as compared to the rectangular ridge waveguides. However, the trapezoidal ridge waveguides have large negative birefringence, and for the given upper ridge width, the birefringence-free point cannot be reached for any choice of etch depth. This is not the case in waveguides with nearly vertical sidewalls, whereas optimal etch depth can be found to satisfy the birefringence-free condition (zero birefringence at $\sim$1.3 $\mu$m). Because it is difficult to precisely control the etch depth due to limitations of the fabrication techniques, methods of controlling birefringence other than modifying waveguide geometry are preferred.

### *B. Upper Oxide Cladding Stress*

Adjusting the stress in the upper cladding layer may be used to eliminate waveguide birefringence [4], [12], [15]. The thickness of the upper cladding can be precisely controlled during fabrication by deposition or etching. Alternatively, the stress in the cladding material can be altered by thermal anneals [4], or by modifying material properties.

Fig. 7 shows the influence of stress on waveguide birefringence for a trapezoidal ridge waveguide with 54° sidewalls for different stress levels in the oxide cladding: $\sigma_{\rm film} = 0, -100,$ $-200$, and $-300$ MPa (for this waveguide, the geometrical birefringence remains at $-0.0015$ and it cannot be eliminated by changing etch depths, see Fig. 6). The birefringence can be effectively modified by varying either the cladding stress $(\sigma_{\rm film})$ or cladding thickness $(t)$. The oxide cladding with a compressive stress induces a positive offset to the geometrical birefringence, giving a tuning range of $4.2 \times 10^{-3}$ for $\sigma_{\rm film}$ of $-300$ MPa. The birefringence-free operation can be achieved for a range of oxide thicknesses and film stresses. In the following, we will examine the influence of cladding stress on ridge waveguide with different cross sections (etch depth and waveguide width).

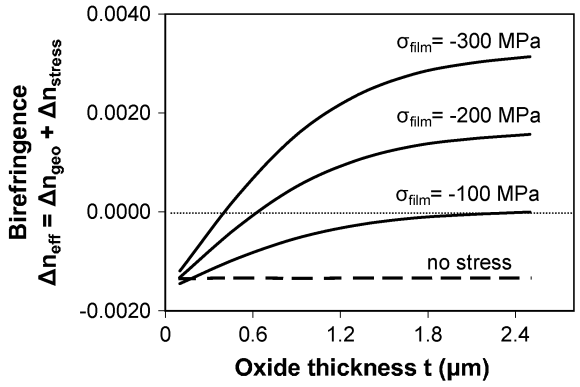


Fig. 7. Influence of upper cladding under different levels of stress on waveguide birefringence. The sidewall slope is 54°, the Si ridge has a width $W_1 = 1.5$ $\mu$m, an etch depth $D = 1.5$ $\mu$m, and a height of $H = 2.2$ $\mu$m. The bottom curve corresponds to the geometrical birefringence (no stress is included in the calculations of waveguide effective indexes).

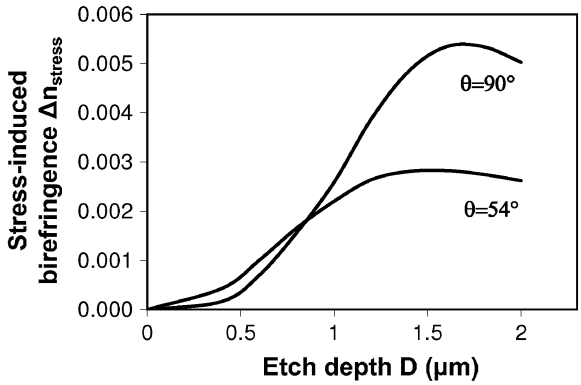


Fig. 8. Etch depth influence on stress-induced birefringence $(\Delta n_{\text{stress}})$ for rectangular $(\theta = 90°)$ and trapezoidal $(\theta = 54°)$ ridge waveguide. The 0.7 $\mu$m upper oxide cladding film is under a compressive stress of $-300$ MPa. The waveguide geometry is identical to that defined in Fig. 6.

*1) Ridge Etch Depth and Stress:* Fig. 8 shows the effects of stress on birefringence with varying etch depths for both rectangular and trapezoidal ridge cross sections under a compressive stress of −300 MPa in the upper oxide cladding. Here the stress-induced birefringence $(\Delta n_{\text{stress}})$ is calculated as the difference between the total waveguide birefringence and the geometrical birefringence (shown in Fig. 6).

As compared to the geometrical birefringence, stress has less influence in total birefringence for shallow etched ridge waveguides. Similar to the geometrical birefringence, the stress-induced birefringence is shown to be less sensitive to the fluctuations in etch depth for deeply etched ridge waveguides. For a core thickness of 2.2 $\mu$m, the relative contribution of the stress-induced effects on total birefringence becomes less sensitive to changes in etch depth for $D$ beyond 1.5 $\mu$m. This is due to the misalignment between the maxima of the electric field (center of the waveguide mode) and the stress field in the core.

*2) Ridge Width and Stress:* Fig. 9(a) compares the effective indexes of TE polarization (with and without stress) for ridge sidewall slopes of 54° and 90°. The effective indexes of TM polarization follow similar trend. The etch depth is fixed at 1.5 $\mu$m, and the core thickness is 2.2 $\mu$m. The effective indexes of the TE modes are reduced under the influence of stress for both the trapezoidal and rectangular ridge waveguides, resulting in birefringence changes. For fluctuations of $\pm 0.1$ $\mu$m in the top ridge width of 1.5 $\mu$m, the change for the dry-etched waveguide (90° sidewall) in the effective index and in the birefringence are $8.4 \times 10^{-3}$ and $1.2 \times 10^{-3}$, respectively. In contrast, the corresponding changes for the wet-etched waveguide (54° sidewall) in $n_{\text{eff}}^{\text{TE}}$ and birefringence $\Delta n_{\text{eff}}$ are $1.5 \times 10^{-3}$ and $7.0 \times 10^{-5}$, respectively. Thus, the ridge waveguides with a trapezoidal cross section are more tolerant to errors in waveguide dimensions.

Fig. 9(b) shows both the geometrical birefringence (dashed curves) and the total birefringence including stress (solid curves) as a function of the ridge width. The birefringence is less sensitive to the ridge width fluctuations for trapezoidal ridge waveguides compared with rectangular waveguides, but trapezoidal ridge waveguides suffer from a large negative geometrical birefringence. As shown in Fig. 9(b) a compressive stress in the upper cladding produces a positive offset in the birefringence profile. With the birefringence offset provided by the stress, zero birefringence condition can now be satisfied even for trapezoidal ridge waveguides. This figure emphasizes that stress can provide an additional parameter in keeping the waveguides free of birefringence.

## IV. Experiments

This section presents the experimental demonstration of the modal birefringence control in SOI waveguides using stress induced by the upper cladding. Experimental results measured in SOI AWG demultiplexers are compared with the results calculated in the previous section.

Test AWG devices were fabricated on SOI $\langle 100 \rangle$ wafers, with a 2.2-$\mu$m-thick Si core layer and a 0.37-$\mu$m-thick buried oxide layer. The devices were designed to operate at a central wavelength of $\lambda = 1550$ nm. The waveguide arrays consist of 100 ridge waveguides with a length increment between adjacent waveguides of 22.68 $\mu$m, corresponding to a grating order of 49. The AWGs had eight input and eight output channels. The overall chip size was approximately 5 mm × 5 mm. The layout of the eight-channel AWG demultiplexer and details of the AWG design can be found in [4], [12], [17], and [18].

The value of the stress level in a blanket thin film $(\sigma_{\text{film}})$ was obtained experimentally by measuring wafer's curvature radius and using the following relation

$$\sigma_{\text{film}} = \frac{Eh^2}{(1-\nu)6Rt} \tag{15}$$

where $E/(1-\nu)$ is the biaxial elastic modulus of the substrate, $h$ is the substrate thickness, $t$ is the film thickness, $R$ is the substrate radius of curvature, and $\sigma_{\text{film}}$ is the average film stress. The bow radii of the wafer before $(R_1)$ and after $(R_2)$ film deposition were first measured. The effective radius of curvature was then obtained by using $R = R_1R_2/(R_1 - R_2)$.

The birefringence of waveguides in the arrayed grating section of an AWG is calculated from the measured polarization dependent wavelength shift $(\Delta\lambda)$ in the AWG demultiplexer [19]:

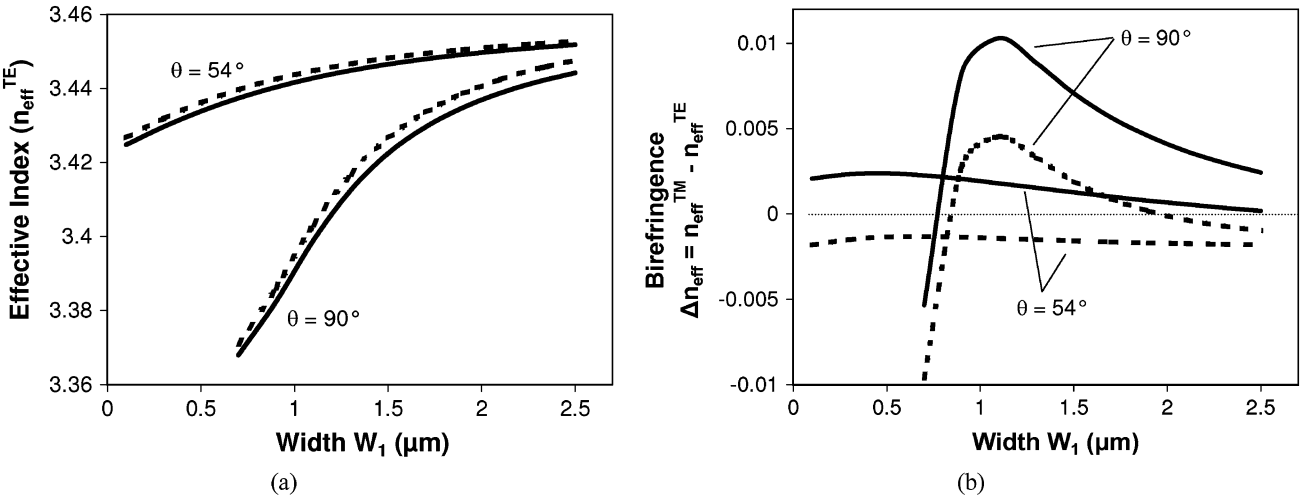


Fig. 9. Ridge width influence on waveguide effective index and birefringence for trapezoidal and rectangular waveguides. (a) Effective mode indexes of TE polarization with stress (solid curves) and without stress (dashed curves) in trapezoidal ($\theta = 54°$) and rectangular ($\theta = 90°$) ridge waveguides. (b) Geometrical birefringence (dashed curves) and total birefringence ($\Delta n_{\rm stress} + \Delta n_{\rm geo}$) under a compressive stress of $\sigma_{\rm film} = -300$ MPa (solid curves). The Si ridge etch depth is 1.5 $\mu$m, and ridge height $H$ is 2.2 $\mu$m.

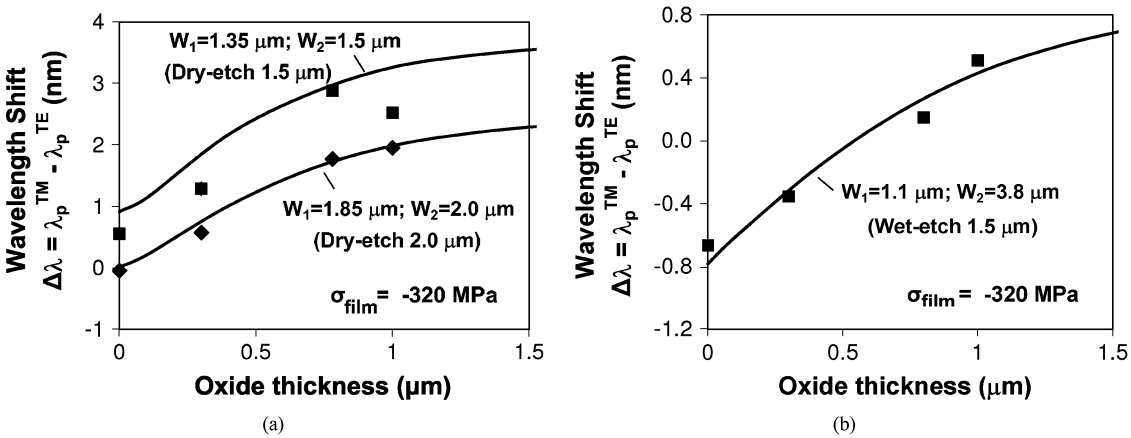


Fig. 10. The measured (data points) and calculated (solid curves: by using the normalized plane-strain model with material parameters listed in Table I) wavelength shift ($\Delta\lambda$) in the demultiplexer's spectra for varying oxide thickness. (a) Dry-etched waveguides (with nominal widths of 1.5 and 2.0 $\mu$m, respectively). (b) Wet-etched waveguides (with nominal widths of 1.5 $\mu$m), with stress of $\sigma_{\rm film} = -320$ MPa. The ridge edge depth was measured as 1.47 $\mu$m. Stress was determined from the measurements on wafer bow radius.

$\Delta n_{\rm eff} = n_{\rm g} \cdot \Delta\lambda/\lambda$, where $n_{\rm g}$ is the group index of the waveguide. Here $\Delta\lambda = \lambda_{\rm peak}^{\rm TM} - \lambda_{\rm peak}^{\rm TE}$ is the shift between the demultiplexer channel peak wavelengths measured for TM and TE polarizations. In these calculations, $\lambda$ and $n_{\rm g}$ are assumed to be 1550 nm and 3.476, respectively.

The ridge waveguides in the arrayed grating area were fabricated using both dry and anisotropic wet etch methods, with designed ridge widths of 1.5 and 2 $\mu$m. The actual ridge dimensions for the waveguides were measured by scanning electron microscope (SEM) at several locations along the waveguide bends in the arrayed grating section. The average measured widths for the dry-etched ridges were $W_1 = 1.35$ $\mu$m (top width) and $W_2 = 1.5$ $\mu$m (bottom width) for a nominal width of 1.5 $\mu$m; and $W_1 = 1.85$ $\mu$m and $W_2 = 2.0$ $\mu$m for a nominal size of 2.0 $\mu$m. The spread in measured ridge widths was within 5% of the average. The measured etch depths for these ridge waveguides were $D = 1.47$ $\mu$m $\pm$ 1%. The wet-etched ridge waveguides, on the other hand, had average measured widths of $W_1 = 1.1$ $\mu$m and $W_2 = 3.8$ $\mu$m for a nominal ridge width of 1.5 $\mu$m; and $W_1 = 1.5$ $\mu$m and $W_2 = 4.0$ $\mu$m for a nominal size of 2.0 $\mu$m. The variation in the width measurements for the wet-etched waveguides can be up to $\pm 20$, depending on the angle relative to the major crystal planes. The etch depths of the wet-etched ridges were measured to be 1.47 $\mu$m $\pm$ 2%.

The oxide upper cladding was then deposited by PECVD in three steps, yielding oxide thickness of 0.3, 0.8, and 1 $\mu$m, respectively. The oxide thickness nonuniformity is normally better than 5%. The polarization dependent wavelength shift $\Delta\lambda$ was measured after each deposition step. The compressive stress measured in the oxide film was $\sigma_{\rm film} = -320 \pm 5$ MPa for both the dry- and wet-etched ridge waveguides. Fig. 10 plots the measured wavelength shift data as a function of the upper cladding thickness averaged over several AWG channels. The dry-etched ridges have slightly slanted sidewalls, as indicated in Fig. 10(a), and the wet-etched ridges have sidewall angles of approximately 54° [shown in Fig. 10(b)]. The solid curves shown in Fig. 10 were the FEM calculations based on the actual measured ridge dimensions.

The expected uncertainty in the calculated birefringence based on the measured device parameters can be estimated using the curves presented in Figs. 6 through 10. Fig. 9(b) shows that small variations in width for narrow rectangular (dry-etched) waveguides result in larger changes in birefringence. A 5% spread around 1.5 $\mu$m in dry-etched ridge widths will result in a 15% spread in birefringence. In a dry-etched ridge waveguide with a 1.5 $\mu$m etch depth, the 1% spread in measured etch depth can result in a 5% spread in birefringence. In contrast, the trapezoidal (wet-etched) and wide (e.g., 2.0 $\mu$m) rectangular ridge waveguides are relatively insensitive to variations in ridge widths. Similarly, variations in etch depth has almost no effect for trapezoidal and deep etched rectangular ridge waveguides, as suggested in Figs. 6 and 8. These considerations explain the close agreement between the simulation results and the experimental data for the wide dry-etched waveguides [bottom curve in Fig. 10(a)] and the wet-etched waveguides in Fig. 10(b).

Overall, there is very good agreement between the simulation results and the experimental data. The scatter in the experimental data is consistent with the small variations in width ($W_1$ and $W_2$), etch depth ($D$) and stress ($\sigma_{\mathrm{film}}$) in the fabricated devices.

## V. Conclusion

We have demonstrated that stress engineering is an effective tool to control waveguide birefringence in SOI waveguide devices, for a wide range of waveguide cross-section shapes and dimensions. A normalized plane-strain model was proposed and used to calculate the stress distribution and the corresponding refractive index distribution in SOI ridge waveguides. Simulations show that this model produces virtually identical results as the fully generalized model, yet requires an order of magnitude less computation time. We examined two types of waveguide cross sections (rectangular and trapezoidal) and studied birefringence as a function of the geometry profiles and stress effects induced by the oxide cladding. Waveguides with trapezoidal ridge cross sections or wider ridge widths offer improved birefringence tolerance to dimension fluctuations. The large geometrical birefringence usually associated with the trapezoidal waveguides can be eliminated by depositing stressed claddings. The numerical simulations and the experimental results confirms that the thickness and the stress level of the upper cladding layer are two useful parameters for effective birefringence tuning. We also demonstrated an application of this technique for the elimination of polarization dependent spectral shifts in SOI AWG demultiplexers. This technique is not restricted only to SOI waveguides, it should be generally applicable for different types of high index contrast platforms and devices.

## References


[1] K. Okamoto, *Fundamentals of Optical Waveguides*. New York: Academic, 2000.

[2] L. Vivien, S. Laval, B. Dumont, S. Lardenois, A. Koster, and E. Cassan, "Polarization-independent single-mode rib waveguides on silicon-on-insulator for telecommunication wavelengths," *Opt. Commun.*, vol. 210, pp. 43–49, 2002.

[3] M. R. T. Pearson, A. Bezinger, A. Delâge, J. W. Fraser, S. Janz, P. E. Jessop, and D.-X. Xu, "Arrayed waveguide grating demultiplexers in silicon-on-insulator," in *Proc. SPIE*, vol. 3593, 2000, pp. 11–18.

[4] D.-X. Xu, P. Cheben, D. Dalacu, S. Janz, M.-J. Picard, N. G. Tarr, and W. N. Ye, "Control and compensation of birefringence in SOI waveguides," in *Proc. 16th Annual Meet. IEEE Lasers Electro-Optics Society (LEOS 2003)*, Oct. 2003, p. 590.

[5] *Landolt-Bornstein: Numerical Data and Functional Relationships in Science and Technology: New Series. Group III, Crystal, and Solid State Physics*, vol. 11, pp. 512–513, 1979.

[6] M. Huang, "Stress effects on the performance of optical waveguides," *Int. J. Sol. Structures*, vol. 40, pp. 1615–1632, 2003.

[7] S. P. Timoshenko and J. N. Goodier, *Theory of Elasticity*, 3rd ed. New York: McGraw-Hill, 1970.

[8] M. Okuno, A. Sugita, K. Jinguji, and M. Kawachi, "Birefringence control of silica waveguides on Si and its application to a polarization-beam splitter/switch," *J. Lightw. Technol.*, vol. 12, no. 4, pp. 625–633, Apr. 1994.

[9] K. Saitoh, M. Koshiba, and Y. Tsuji, "Stress analysis method for elastically anisotropic material based optical waveguides and its application to strain-induced optical waveguides," *J. Lightw. Technol.*, vol. 17, no. 2, pp. 255–259, Feb. 1999.

[10] X.-Z. Zhao, Y.-Z. Xu, and C. Li, "Birefringence control in optical planar waveguides," *J. Lightw. Technol.*, vol. 21, no. 10, pp. 2352–2357, Oct. 2003.

[11] K. Röll, "Analysis of stress and strain distribution in thin films and substrates," *J. Appl. Phys.*, vol. 47, pp. 3224–3229, 1976.

[12] W. N. Ye, D.-X. Xu, S. Janz, P. Cheben, A. Delâge, M. Picard, B. Lamontagne, and N. G. Tarr, "Stress-induced effects on birefringence for silion-on-insultor (SOI) waveguides," in *Proc. SPIE Int. Soc. Opt. Eng.*, San Jose, CA, Jan. 2004, pp. 57–66.

[13] D.-X. Xu, P. Cheben, D. Dalacu, A. Delâge, S. Janz, B. Lamontagne, M. Picard, and W. N. Ye, "Eliminating the birefringence in silicon-on-insulator ridge waveguides using the cladding stress," *Opt. Lett.*, vol. 29, no. 20, pp. 2384–2386, 2004.

[14] D.-X. Xu, J.-M. Baribeau, P. Cheben, D. Dalacu, A. Delâge, B. Lamontagne, S. Janz, M. Picard, and W. N. Ye, "Prospects and challenges for microphotonic waveguide components based on Si and SiGe," in *SiGe: Materials, Processing, Devices Symp., Proc. Electrochemical Soc. (ECS '04)*, vol. 2004-07, Oct. 2004, pp. 619–633.

[15] D.-X. Xu, P. Cheben, S. Janz, and D. Dalacu, "Control of SOI waveguide polarization properties for microphotonic applications," in *Proc. 5th CLEO-Pacific Rim*, Dec. 2003, p. 5.

[16] R. A. Soref, J. Schmidtchen, and K. Petermann, "Large single-mode waveguides in GeSi–Si and Si-on-$SiO_2$," *IEEE J. Quantum Electron.*, vol. 27, no. 8, pp. 1971–1974, Aug. 1991.

[17] P. Cheben, A. Bezinger, A. Delâge, L. Erickson, S. Janz, and D.-X. Xu, "Polarization compensation in silicon-on-insulator arrayed waveguide grating devices," in *Proc. SPIE*, vol. 4293, 2001, pp. 15–22.

[18] P. Cheben, D.-X. Xu, S. Janz, and A. Delâge, "Scaling down photonic waveguide devices on the SOI platform," in *Proc. SPIE*, vol. 5117, 2003, pp. 147–156.

[19] S. Janz, "Silicon-based waveguide technology for wavelength division multiplexing," in *Silicon Photonics*, L. Pavesi and D. Lockwood, Eds. Berlin, Germany: Springer-Verlag, 2004, ch. 10.



**Winnie N. Ye** received the B.Eng. and M.A.Sc. degrees in electrical engineering from Carleton University, Ottawa, ON, Canada, and the University of Toronto, ON, Canada, in 2000 and 2002, respectively. Her M.A.Sc. research involved the investigation of nonlinear Bragg grating devices in all-optical signal processing.

She is currently working toward the Ph.D. degree at Carleton University. She is working on polarization management in microphotonic devices in high index contrast waveguide systems at the National Research Council of Canada.

**Dan-Xia Xu** received the Ph.D. degree from Linköping University, Sweden, in 1991, for work on silicon-germanium electronic components such as HBTs.

She is a Research Officer with the National Research Council of Canada (NRC), and also an adjunct professor with the Department of Electronics, Carleton University, Ottawa, ON, Canada. Since joining NRC, her research areas covered the material research, design, and fabrication of optoelectronic and microelectronic components based on silicon, silicon-on-insulator, silicon-germanium alloys, and silicides. In 2001–2002, she was part of the research team of Optenia, Inc., that successfully developed the first glass waveguide echelle grating demultiplexer. Her current research focuses on high index contrast waveguide systems, polarization management, and related passive and active integrated optics.

**Siegfried Janz** received the Ph.D. degree in physics in 1991 from the University of Toronto, Canada. His work focused on surface nonlinear optics.

He joined the National Research Council (NRC) of Canada where he worked on nonlinear frequency conversion and optical switching in III-V semiconductor waveguides and silicon-based optoelectronics. In 2001–2002, he was part of the research team of Optenia Inc. that successfully developed the first glass waveguide echelle grating demultiplexer. He is presently with the Optoelectronic Devices Group, Institute for Microstructural Sciences, NRC, and also an adjunct professor with the Department of Electronics, Carleton University, Ottawa, ON, Canada. His current research interests include active and passive integrated optics, and in particular, microphotonic devices in high index contrast waveguide systems.

**Pavel Cheben** received the M.S. degree in microelectronics and optoelectronics from the Slovak Technical University, Bratislava, Slovakia, in 1989 and the Ph.D. degree in physics from the Universidad Complutense, Madrid, Spain, in 1996.

He was previously with the National Institute for Aerospace Technology of Spanish Ministry of Defense, where he led the establishment of the Laboratory of Space Instrumentation. He is currently a Research Officer with the National Research Council (NRC) of Canada, and also an adjunct researcher with the Department of Physics, Complutense University of Madrid. His research interests encompass integrated optics, photonics, and experimental optics, particularly silicon photonics, microphotonic components and devices in high index contrast waveguides, and photonic and optical materials. In 2001–2002, he was part of the research team at Optenia, Inc., that successfully developed the first glass waveguide echelle grating demultiplexer.

**Marie-Josée Picard** received the M.Sc. degree in electrical engineering from Laval University in 2000. Her thesis concerned a tunable Er:Yb glass laser.

From 1999 to 2002, she was with JDS Uniphase working on several WDM components. She is currently with the Optoelectronic Devices Group, Institute for Microstructural Sciences, National Research Council (NRC) of Canada, working on microphotonics projects.

**Boris Lamontagne** received the Ph.D. degree in engineering physics (surface science) from École Polytechnique, Montréal, Canada, in 1992. Postdoctoral studies were carried out in France and at Laval University.

In 1995, he joined the Institute for Microstructural Sciences, National Research Council (NRC) of Canada (NRC). He is also an adjunct professor with Carleton University, Ottawa, ON, Canada. In 2001–2002, he was a member of the team which started-up Optenia, Inc., and developed the Echelle grating demultiplexer on silica. He rejoined the NRC in 2002. His current interests are the fabrication of novel planar waveguide devices and the development of dry-etching processes.

**N. Garry Tarr** was born in Vancouver, BC, Canada, in 1956. He received the B.Sc. degree in physics and the Ph.D. degree in electrical engineering from the University of British Columbia in 1977 and 1981, respectively.

He has served as a faculty member with the Department of Electronics, Carleton University, Ottawa, ON, Canada, since 1982, and currently holds the rank of Professor. His general research interests are in silicon process technology and device physics. His research has recently focused on integrated optoelectronic devices in silicon-on-insulator substrates.